Questioning the Representativeness of Damage Mechanisms in Single-Fiber Composites via *In-situ* Synchrotron X-ray Holo-tomography

Thanasis Chatziathanasiou[*, a], Yeajin Lee[b], Julie Villanova[c], Olga Stamati[c], Sina AhmadvashAghbash[a], Babak Fazlali[a], Christian Breite[a], Ian Sinclair[b], Mark N. Mavrogordato[b], S. Mark Spearing[b], Mahoor Mehdikhani[a], Yentl Swolfs[a]

[a] *KU Leuven, Department of Materials Engineering, Leuven, Belgium*

[b] *University of Southampton, μ-VIS X-ray Imaging Centre, Southampton, UK*

[c] *ESRF, The European Synchrotron CS 40220 38043 Grenoble Cedex 9, France*

Keywords: Synchrotron holo-tomography, *In-situ* damage monitoring, Polymer composites, Interfacial properties

Abstract

In fiber-reinforced polymer composites, the fiber-matrix interface controls stress transfer mechanisms, thereby affecting mechanical performance. Interfacial properties are often extracted via single-fiber composite tests. In these tests, the load is transferred from the polymer to the fiber through interfacial shear stresses, necessitating the evaluation of interfacial shear properties. To adopt these properties in the design of industrially relevant composites, one must assume that the damage mechanisms in single-fiber composites are representative of those in multi-fiber composites, consisting of highly aligned, unidirectional plies with high fiber volume fractions. That assumption, however, has never been validated. In this paper, we monitor the real-time damage development in single-fiber and multi-fiber composites using *in-situ* X-ray holo-tomography at 150-nm pixel size. The technique enables the first-ever 3D detection of longitudinal interfacial debonding in carbon and glass single-fiber composites. This mechanism is not detected in multi-fiber composite specimens, suggesting that single-fiber composites are intrinsically unrepresentative of realistic composite behavior.

Introduction

Fiber-reinforced polymer composites offer design flexibility, multifunctionality, and excellent specific mechanical properties, leading to widespread use in sectors such as aerospace, automotive, energy, and construction. Three length scales describe the hierarchical structure of composites: micro- (1 to 100 μm), meso- (100 μm to a few mm), and macroscale (1 cm to meters). The microscale is associated with the constituents, namely fiber, matrix, and interface, whose properties govern the mechanical performance of composites across all higher scales. Considerable efforts have been devoted to studying and quantifying the properties of these constituents, including the use of *in-situ* tests [1]. However, the interface has been

[*] Corresponding author: thanasis.chatziathanasiou@kuleuven.be

particularly challenging to reliably characterize due to its small characteristic length and sensitivity to the local chemistry and microstructure.

The interface is key in transferring stress between the fiber and the matrix. The interfacial shear strength, fracture toughness, and friction coefficient are often used to characterize stress transfer efficiency. Direct micromechanical test methods have been developed to extract these properties [1]. Most tests, such as the single-fiber fragmentation [2], single-fiber pull-out [3], and microbond [4], utilize single-fiber composites. In such tests, an isolated fiber is either fully or partially embedded in the polymer matrix. Interfacial tests such as the fiber push-in/-out tests that are applied to *multi-fiber* composites are much scarcer [5], mainly because of the tedious sample preparation required. The term *multi-fiber* refers to industrially relevant composites with many fibers at fiber volume fractions ranging from 40 to 75%. Unfortunately, a round-robin exercise among different labs and test methods showed large differences in the measured values of the interfacial shear strength for the same material system [6].

One key factor driving the discrepancies may be the lack of mechanistic consistency or representativeness of single-fiber composites compared to multi-fiber composites. Naturally, the assumption of representativeness neglects the interactions between neighboring fibers and the so-called "*in-situ* effect" of the matrix, meaning that the polymer mobility and curing process may be affected by the presence of fibers, altering local matrix properties and material chemistry (chemical bonding) adjacent to the interface [7]. Numerical studies also reported that the local stress state around a fiber is influenced by the presence of neighboring fibers [8, 9]. In general, the representativeness of the single-fiber tests has never been validated.

Since the 1950s, many theoretical models have been proposed for the stress transfer at the fiber-matrix interface [10-12]. As these models became more complex and comprehensive, the need for their experimental validation became more pronounced [8]. The experiments, however, have not caught up with the progress in modeling. Most setups remain based on *in-situ* testing with optical microscopy [13]. Unfortunately, optical microscopy is always limited by its resolution, which is insufficient to detect interfacial debonding directly. Furthermore, it is necessarily limited to fibers which are at the surface of a specimen, or are optically accessible via a transparent matrix. Indirect detection is possible via polarised light and cross-polarisers, but this is not always straightforward to interpret [14]. However, without reliably detecting the debond, the interpretation and quantification of interfacial properties remain questionable. This compromises the reliability of micromechanical models and highlights the importance of high-resolution 3D visualization tools for identifying and quantifying interface debonding.

X-ray computed tomography is a key method for non-destructive 3D imaging. The highest resolution is achieved via Synchrotron Radiation Computed Tomography (SRCT), where the X-rays are produced by the electrons circulating through a synchrotron storage ring [15]. Typically, SRCT offers a unique combination of fast acquisition and high spatial resolution. Swolfs, Schöberl et al. [16, 17] exploited these features to

investigate fiber break accumulation in carbon fiber composites under quasi-static tensile loading, while Garcea et al. [18, 19] investigated the damage propagation under fatigue loading for the same fiber type. While these studies shed new light on microscale damage development in composites, they did not study the role of the interface. Studying the interface was not feasible because cracks cannot be detected without a significant crack opening on the order of one-third of the pixel size [20]. Specifically, a 650 nm pixel size was inadequate to visualize interface debonds, which, if present, would have a negligible crack opening [17]. Higher resolutions than 650 nm are rarely used in SRCT studies on composites due to the need to compromise between resolution and field of view, as well as limits on the X-ray optics at most beamlines [21].

To overcome the imaging limitations, we conducted *in-situ* holo-tomography tests at the ID16B beamline at the European Synchrotron Radiation Facility (ESRF) at a 150-nm pixel size. This corresponds to a fourfold improvement compared to previous experiments, allowing debonds to be detected by propagation-based X-ray phase contrast nano-imaging. The tests were designed to investigate debonding in both single-fiber and multi-fiber composites. The two most industrially-relevant fiber types were scrutinized: carbon and glass fiber.

Results

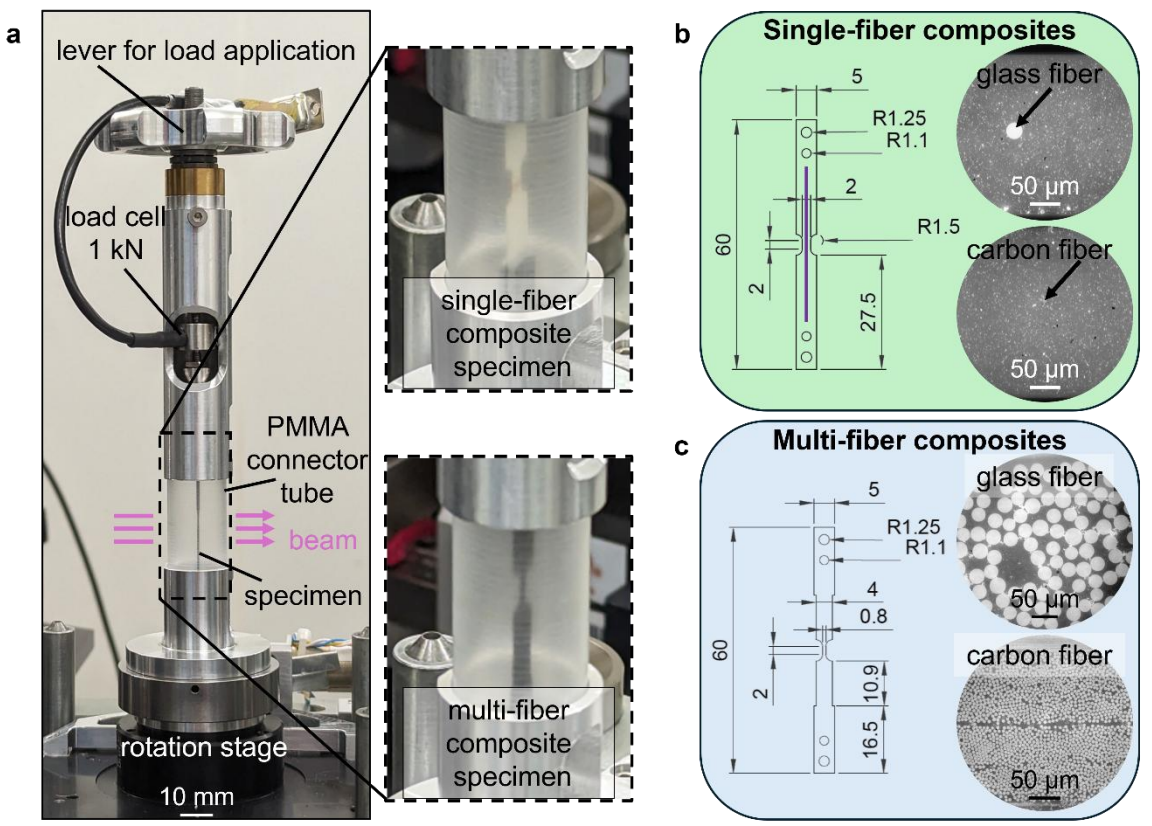

Figure 1 Synchrotron holo-tomography experimental setup and investigated specimen cases. (a) *In-situ* loading rig mounted on the rotation stage of ID16B, along with magnified section indicating the notched single-fiber and multi-fiber composite specimens, (b) drawing of the single-fiber specimen indicating the embedded fiber in purple and with representative reconstructed SRCT slices for glass and carbon single-fiber composites, and (c) drawing of the multi-fiber composite specimens with representative reconstructed SRCT slices for glass and carbon multi-fiber composites. The drawing dimensions are in mm.

Holo-tomography scans were acquired for each single-fiber and multi-fiber composite specimen at distinct load steps, corresponding to fractions of the nominal ultimate tensile strength (UTS). Figure 1a presents the

in-situ loading rig used, while Figure 1b and Figure 1c display the specimen geometries with representative SRCT slices. After scan reconstruction, the analysis qualitatively describes the occurring damage mechanisms, namely (a) fiber breakage, (b) interfacial debonding, and (c) matrix cracking. A dedicated sub-section for each fiber type (carbon or glass) and configuration (single-fiber or multi-fiber) is provided. Furthermore, the observed mechanisms in single-fiber composites are expressed quantitatively via a list of parameters (see Table 1) to provide direct and essential input into micromechanical models.

Table 1 Damage parameters extracted from the SRCT data of *in-situ* tests of single-fiber composites. Parameters with non-dimensional units are normalized by the respective fiber diameter.

	Glass single-fiber composite				**Carbon single-fiber composite**			
Pixel size [nm]	150				150			
Field of view [px^2]	3846 × 2048				2048 × 2048			
Fiber diameter [µm]	28.3				6.8			
	Fiber break							
Back-calculated stress [%UTS]	**23**	**68**	**92**	**94**	**26**	**65**	**85**	**95**
Number of breaks	0	1	2	2	0	0	1	1
Apparent critical length, normalized [-]	-	-	15.8	15.8	-	-	*	*
*Apparent critical length cannot be measured as there is only one fiber break within the field of view;								
	Longitudinal debond							
Debond length, normalized [-]	0	0	D1 = 2.9 D2 = 1.8	D1 = 6.7 D2 = 4.6	0	0	9.0	34.4
Interdebond length, normalized [-]	-	-	11.1	4.4	-	-	-	-
	Matrix crack							
Crack volume [µm^3]	0	V = 350	V = 14250	V = 24300	-	-	-	-
Max. transverse propagation [-]	0	$T1_a$ = 0.35 $T1_b$ = 0.10 $T1_c$ = 0.07	$T1_a$ = 0.42 $T1_b$ = 0.18 $T1_c$ = 0.07 $T2_a$ = 0.49 $T2_b$ = 0.21 $T2_c$ = 0.14	$T1_a$ = 0.56 $T1_b$ = 0.25 $T1_c$ = 0.14 $T2_a$ = - $T2_b$ = 0.28 $T2_c$ = -	-	-	-	-

Detected damage mechanisms in glass single-fiber composites

Figure 2 depicts the 3D damage development in the tested glass single-fiber composite over four loading steps: 23%, 68%, 92% and 94% of the specimen's UTS. At 23%UTS, the fiber and the surrounding matrix are intact (Figure 2a). The first failure mechanism, a fiber break, appears in the scan acquired at 68%UTS, indicated as B1 in Figure 2b. This implies that the break has occurred somewhere between 23% and 68%UTS. Careful examination of the four propagation distance scans via which the tomogram is constructed reveals that this fiber break occurs during the holo-tomography acquisition, as it only appears in the last distance scan.

The fiber fracture does not occur perpendicular to the fiber direction but rather in two inclined planes. Such wedge or angled fracture patterns have previously been observed for E-glass fibers [22, 23]. Adjacent to the fiber break, a matrix crack initiates from the intersection of the two fracture planes ($T1_a$ in Figure 2b). This load step did not reveal any visible interfacial debonding.

At 92%UTS, a second fiber break emerges (B2 in Figure 2c). The presence of two fiber breaks within the field of view (FOV) allows the extraction of the apparent critical length (l_c), an essential parameter for measuring interfacial shear strength [24, 25]. The critical length is the mean fiber (segment) length upon saturation, the state at which the fiber segments can no longer build up enough stress to fragment further. In this study, this is referred to as the "apparent" critical length since there is no information on whether or not saturation has been reached. Short matrix cracks are visible adjacent to both fiber breaks. Due to the wedge shape of the fiber breaks, the cracks develop laterally in three directions (T_a, T_b, *and* T_c), as seen in Figure 2c. The most extensive crack initiates from the side where the fracture planes converge (T_a). The fracture planes diverge on the other side of the fiber, causing two smaller cracks (T_b, T_c).

Strikingly, interfacial debonds (D) are also evident in the acquired scans of 92% and 94%UTS, extending longitudinally from both fiber breaks. The debonds are relatively symmetric to the fiber axis but do not appear uniformly across the entire fiber circumference (see XY slice in Figure 2c,d). The difference between the YZ and XZ slices also demonstrates this nonuniformity (Figure 2c,d). Since the scans allow accurate 3D debond monitoring, we propose characterizing an additional parameter, the interdebond distance (l_{id}), which is the intact distance between two adjacent debond ends. We argue that this parameter provides the means to validate the *ineffective length*, which is typically defined as twice the axial distance needed for a broken fiber to recover 90% of the nominal stress [9].

At 94%UTS, no new fiber breaks appear within the FOV. The higher applied load has significantly increased the opening of the two existing fiber breaks, causing both break sites and the associated matrix cracks to move partially out of the FOV (Figure 2d). The longitudinal debonds have also grown remarkably at this stage. However, they maintain the same symmetry and nonuniformity as observed at 92%UTS.

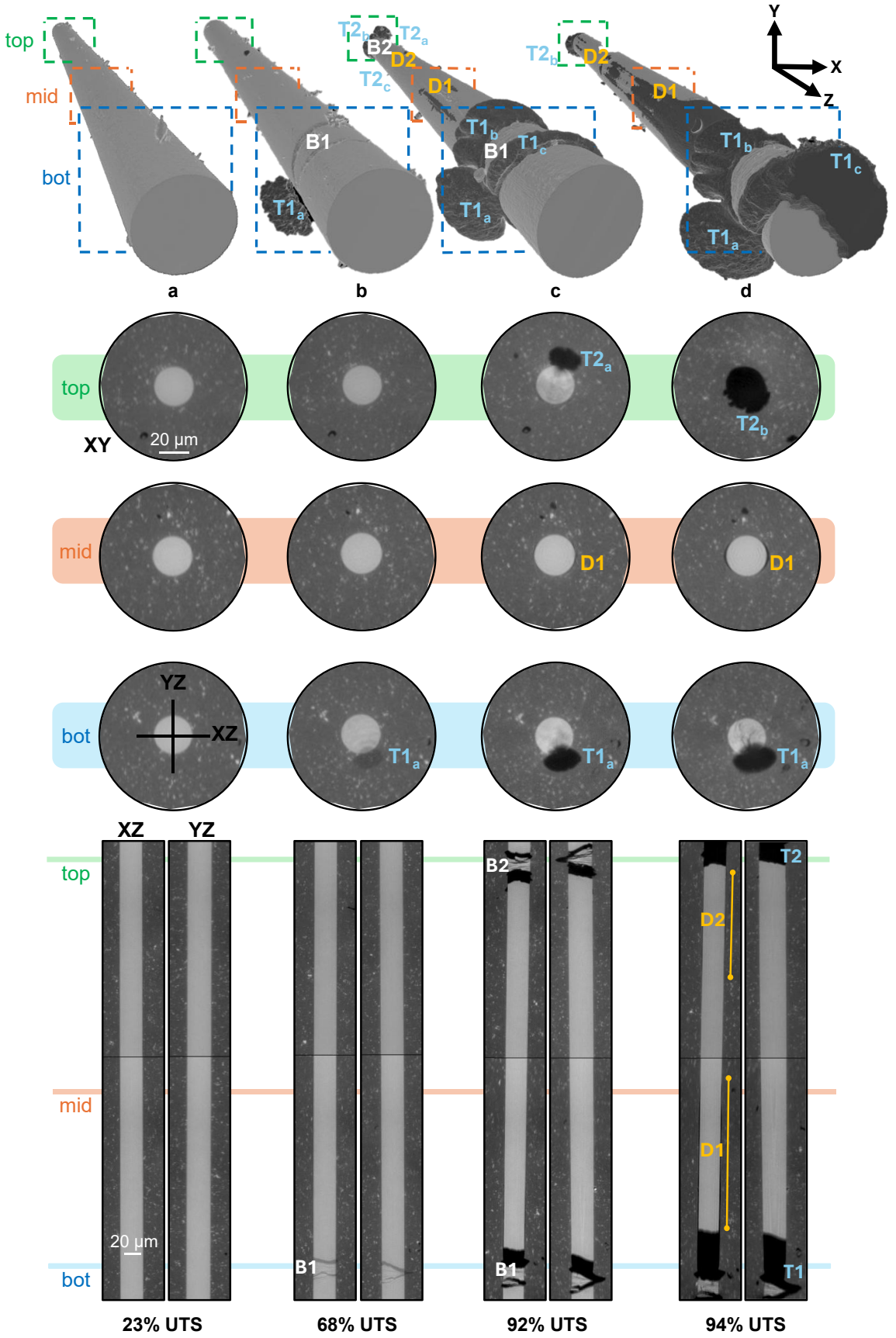

Figure 2 4D damage development analysis in the glass single-fiber specimen via 3D rendering of the segmented reconstructed image and complementary 2D reconstructed greyscale slices. (a) 23%UTS: intact fiber, (b) 68%UTS: occurrence of first fiber break with associated matrix crack (Tn), (c) 92%UTS: second fiber break, matrix crack growth and interfacial debond initiation (D_n), (d) 94%UTS: propagation of the same damage mechanisms. For the 2D slices: XY – longitudinal plane, XZ – frontal plane, and YZ - transverse plane; the color distinction of the XY slices (green, orange, and blue) indicates their corresponding XY plane, visualized as dashed rectangles on the 3D rendering.

Detected damage mechanics in carbon single-fiber composite

Figure 3 presents the identified damage in the carbon single-fiber composite over four loading steps: 26%, 65%, 85%, and 95%UTS. No damage mechanisms were observed at 26% and 65%UTS (Figure 3a, b). The first fiber break is detected in the 85%UTS scan (Figure 3c). In contrast to the wedge-shaped fiber break pattern in the glass fiber specimen, the carbon fiber break appears in one plane perpendicular to the fiber direction. The fracture pattern is relatively smooth and featureless. We hypothesize that the difference in crack formation behavior primarily arises from the fibers' intrinsic nanostructure and mechanical properties. PAN-based carbon fibers possess a semi-crystalline skin and core structure [26]. The skin is stiffer and stronger than the core yet is prone to surface defects that can trigger sudden failure. Since the core might offer relatively low resistance to crack propagation, the crack could easily propagate in the plane perpendicular to the induced load. In contrast, glass fibers have an amorphous nanostructure. Crack branching and bifurcation phenomena have been previously observed in amorphous materials, yet are not fully understood [27]. The fracture in such materials typically follows the path of shear bands with an angle to the loading direction [28].

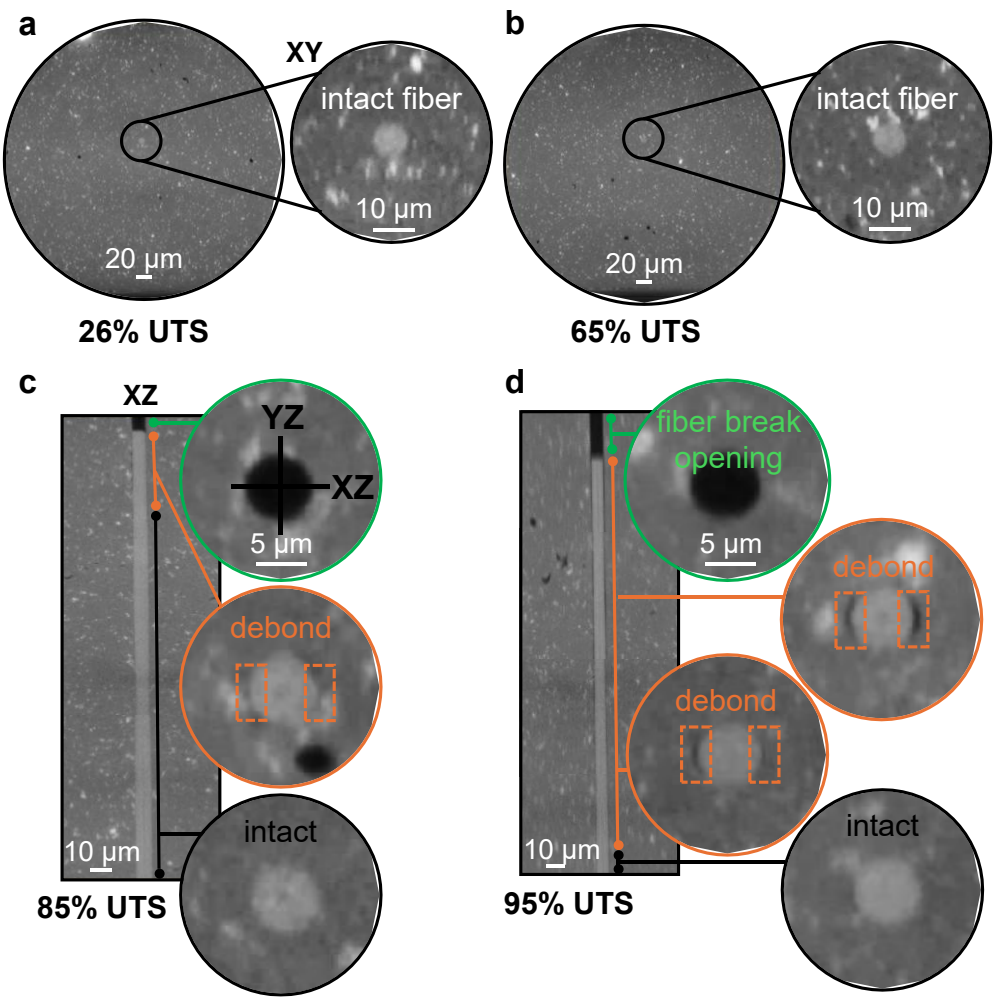

Figure 3 Evolution of damage mechanisms in the carbon single-fiber specimen. (a) XY slice of intact fiber at 26%UTS, (b) XY slice of intact fiber at 65%UTS, (c) XZ slice acquired at 85%UTS showing a fiber break at the top of the FOV, causing a longitudinal debonding zone extending 9 fiber diameters (=61 µm) from the break site in the absence of matrix cracking, (d) XZ slice acquired at 95%UTS indicating growth of the debonded region, which now extends 34.4 fiber diameters (=234 µm) from the break site.

An interfacial debond is seen developing from the fiber break (Figure 3c). Similar to the glass single-fiber specimen, the debond is relatively symmetric considering the fiber axis, yet nonuniform around the fiber's circumference. Unlike the glass fiber case, no matrix cracks were observed, including at 95%UTS, where the debond grows further without the occurrence of a matrix crack (Figure 3d).

Multi-fiber composites damage behavior – Glass fiber

The fiber volume fraction for the glass multi-fiber composite was 42.4%. Within the FOV, the measured fiber diameter was within [21.1, 28.8] μm with an average of 24.5 ± 1.6 μm (nominal diameter = 24 μm). The analysis loading steps are 7%, 35%, 55%, 82%, and 90%UTS. The first fiber breaks (five in total) appear at 82%UTS. They occur in random locations across the FOV and are not part of a cluster (Figure 4a). Similar to [17], we define a cluster as a collection of fiber breaks separated by less than ten fiber diameters longitudinally (*Z*) and two fiber diameters radially (*X* and *Y*). *Z* is measured from the center of the respective fiber break openings, while the X and Y are calculated using the center of the respective fibers. Figure 4b shows that fiber breaks have the same characteristic wedge shape observed in the glass single-fiber composite. In the multi-fiber composite, however, the presence of other fibers in the vicinity of a break restricts the development of matrix cracks, which appear negligible (Figure 4b) but were significant in the glass single-fiber case (Figure 2c-d). In addition, interfacial debonding is not detected anywhere within the FOV.

Three more fiber breaks are detected at 90%UTS (Figure 4c). In this case, they are associated with two clusters, one triplet (= three interacting fiber breaks) and one duplet (= two interacting fiber breaks). Considering the cluster definition, these two clusters are not interacting. However, it should be noted that the damaged region is located at the edge of the FOV, meaning that possibly more fiber breaks are located next to the ones visible, but outside the FOV. This is a limitation of the very high resolution used in the current work, which is required for the desired level of detail and accuracy. The trends observed at 82%UTS are repeated at the higher load: no interfacial debonding is evident, while matrix cracking remains negligible despite a significant increase in fiber break opening (Figure 4d versus Figure 4b). Namely, the largest matrix crack observed across all fiber breaks in the glass multi-fiber composite is approximately four times smaller than in the glass single-fiber composite (= 0.08 versus 0.42 fiber diameters) when similar global stress levels are considered (90% versus 92%UTS).

Multi-fiber composites damage behavior – Carbon fiber

The fiber volume fraction for the carbon multi-fiber composite was 48.5%. The measured fiber diameter was within [4.9, 6.2] μm with an average of 5.5 ± 0.3 μm (nominal diameter = 5.4 μm). The analysis loading steps are 5%, 67%, 86%, 91% and 96%UTS. The first damage is detected at 67%, corresponding to a duplet most likely caused by local fiber misalignment at the 0°/0° ply interface. At 86%UTS, 25 fiber breaks are detected within the FOV. From these, 13 emerge in a resin-rich area indicated in green in the XY slice of Figure 4e. Within that area, local fiber misalignment was also evident. Eight fiber breaks emerge adjacent to

the 0°/0° interface, while two emerge adjacent to the 0°/90° interface. The remaining two fiber breaks are isolated. Most fiber breaks are not co-planar within the cluster, although we did find three cases of co-planar duplets (two in the resin-rich area and one adjacent to the 0°/0° interface). The fracture surfaces appear planar, as observed in the carbon single-fiber specimen. However, no interfacial debonding is detected in the multi-fiber composite, and, as for the single fiber case, no matrix cracking is observed either.

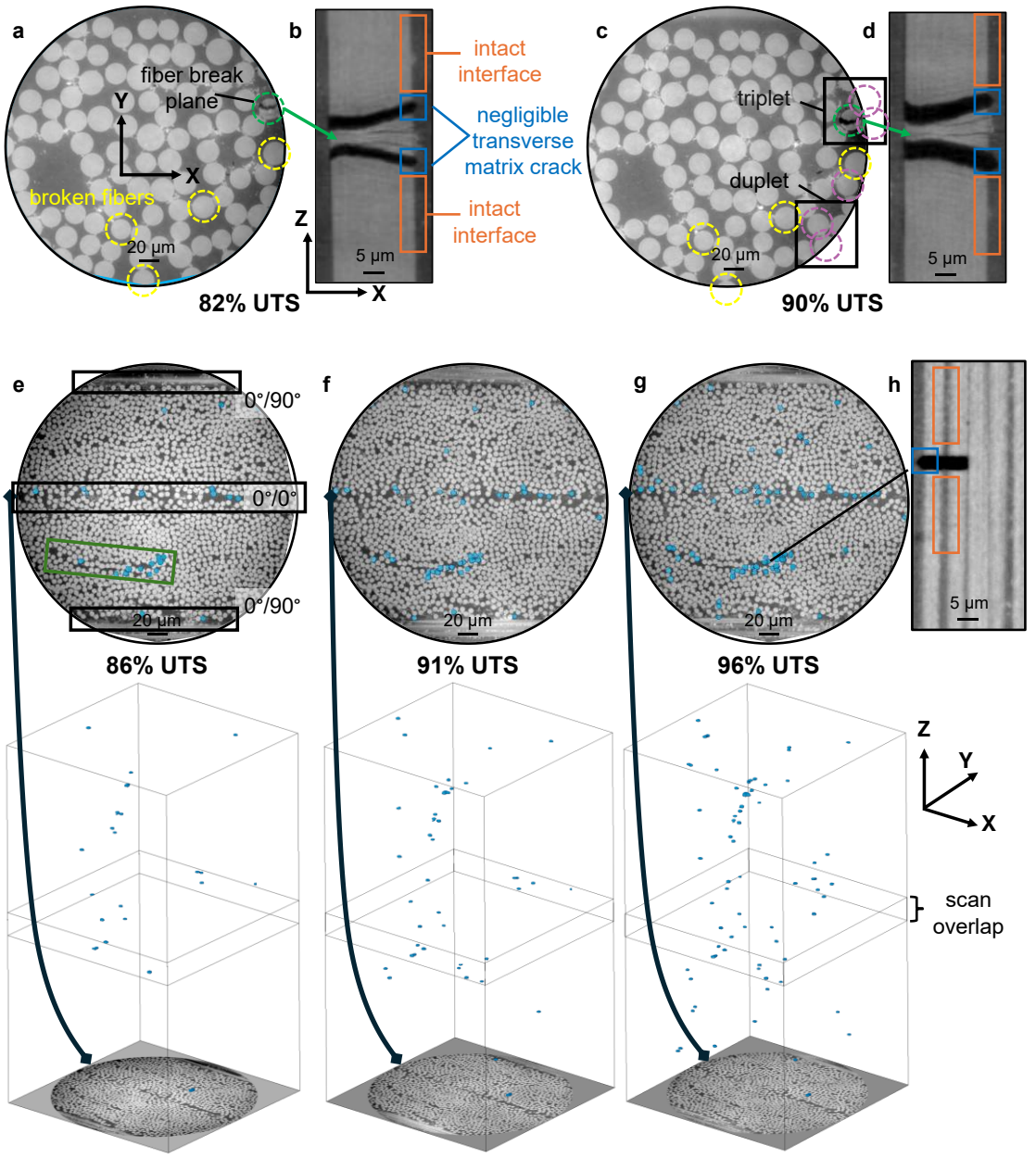

Figure 4 Damage development in multi-fiber glass and carbon composites. (a) Glass fiber XY slice acquired at 82%UTS, where the isolated fiber breaks are designated in yellow; the fiber breaks are not co-planar, hence the XY slice only shows one individual fiber break plane (shown in green), (b) XZ slice indicating the same fiber break exhibiting the characteristic wedge shape as observed for glass single-fiber composites, this time without visible matrix cracking and interfacial debonding, (c) Glass fiber XY slice acquired at 90%UTS, where fibers corresponding to the newly developed fiber breaks are designated in purple; the black rectangles highlight areas of break cluster formation, (d) XZ slice indicating the evolution of the same fiber break as seen in (b), maintaining intact interfaces in the adjacent matrix, (e) Carbon fiber XY slice at 86%UTS with fiber breaks shown in blue and the 3D visualization of the identified fiber breaks in the entire FOV, the black rectangles highlight the ply interfaces while the green rectangle highlights the resin-rich area, (f) evolution of carbon fiber breaks at 92%UTS, and (g) 96%UTS, (h) XZ slice indicating negligible matrix cracking and absence of visible debonding in a co-planar fiber break duplet, as visualized at the highest acquired loading state of 96%UTS.

A pronounced increase in fiber breaks is noted in the 91% (Figure 4f) and 96%UTS (Figure 4g) scans, with 46 and 76 fiber breaks present within the FOV, respectively. At 91%UTS, out of 46 fiber breaks, 20 are located in the resin-rich area (one co-planar triplet, one co-planar duplet), 16 are adjacent to the 0°/0° interface (one co-planar duplet), four are adjacent to the 0°/90° interface, with the remaining six fiber breaks being isolated in the intraply region. At 96%UTS, out of 76 fiber breaks, 27 are in the resin-rich area (one co-planar quadruplet, one co-planar duplet), 26 at the 0°/0° interface (four co-planar duplets), five are present next to the 0°/90° interface, with 18 isolated in the bulk of the 0° plies (3 co-planar duplets).

The lack of detectable debonding and cracking persists in both loading steps. If open debonds were to be present, they would appear as lines along the Z-axis of the 2D visualizations that would extend on either side of each fiber break or, in the case of Figure 4h, on either side and within the interfiber area of the co-planar duplet. Similarly, matrix cracking would be visualized as lines along the X-axis. However, as seen in Figure 4h, only a negligible extension of the break is seen progressing into the matrix.

Conclusions

We investigate microscale damage development in single-fiber and multi-fiber composites. *In-situ* tensile tests are conducted for the two most technologically relevant fiber types, carbon and glass, in conjunction with X-ray synchrotron holo-tomography. By testing both single-fiber and multi-fiber composites, we investigate the suitability of single-fiber composites in offering a mechanistically viable specimen to extract the interfacial properties of commercially produced fiber-reinforced composites. This investigation only becomes feasible at ultra-high resolutions with the use of holo-tomography since it hinges on detecting sub-microscale damage mechanisms acting upon the fiber-matrix interface. Therefore, in this study, the tests are conducted at the ID16B beamline at ESRF, where nano-tomography scans are acquired across a large load spectrum (ranging from near-zero load to close to ultimate failure) at 150-nm pixel size. The experiments enable the first-ever 3D detection and monitoring of longitudinal debonds in carbon and glass single-fiber composites. However, this damage mechanism is not observed in multi-fiber composites. This absence raises questions concerning the calculated values of interfacial properties using single-fiber testing methods.

In general, during single-fiber composite testing, such as fragmentation testing, the energy released from a fiber break is transferred to the surrounding material, causing longitudinal interfacial debonding and/or matrix cracking. The severity of each mechanism depends on the interface and the matrix properties [1]. For instance, a weak interface would typically be subjected to extensive debonding and minimum cracking since that mechanism provides the path of least resistance for energy release. In contrast, a strong interface would divert the energy towards forming matrix cracks. Although, in principle, the same energy transfer mechanisms do occur in multi-fiber composites as in single-fiber composites, our observations indicate that, mechanistically, the two specimens, although comprised of the same constituents, are very different. While we are not yet sure of the reasons driving these differences, we do have a few hypotheses:

- Matrix size effect: Studies have shown that the strength and failure strain of thermosetting matrices exhibit a size dependency, meaning that the smaller the volume, the higher the strength and failure strain, respectively [29, 30]. This may have implications in our study since the matrix volume in single-fiber composite specimens is still orders of magnitude larger than the respective matrix volume inside a multi-fiber composite, where interfiber spacings are below one μm. This, in turn, could influence the *in-situ* damage behaviour.
- Interphase or *in-situ* matrix effect: No conclusive knowledge exists regarding the influence of fibers on the curing, bonding and molecular arrangement of the polymer. This is often referred to as the interphase effect in the literature, whereby the matrix near the fiber surface has properties distinct from the bulk matrix [31].
- Fiber volume fraction effect: Our observations indicate that both debonding and matrix cracking are absent or negligible in multi-fiber composites. This could be attributed to the higher stiffness environment, which hinders large deformations and restricts the development of cracks.
- Thermal expansion differences: In carbon and glass fiber composites, the fibers have a lower coefficient of thermal expansion (CTE) than the polymer matrix. This results in a larger average mismatch strain in the single-fiber composite, and, depending on the local volume fraction and microstructure, may result in differences in the effective radial clamping pressure, which may suppress, or enhance, debonding.
- Energy release upon fiber fracture: When a multi-fiber composite is loaded, the final failure is governed by the average fiber strength. In contrast, in a single-fiber composite, failure is primarily controlled by the polymer. As a consequence, fiber failure occurs at a much higher strain and strain energy in a single-fiber than a multi-fiber composite. This hypothesis is supported by the fact that the single-fiber specimens exhibit two fiber breaks within the FOV. This phenomenon was never observed in the multi-fiber composites, for which we observed a maximum of a single break per fiber. According to our estimates, the strain energy at fiber failure was approximately seven times higher in the single-fiber case. This higher strain energy needs to be absorbed as some type of damage and this could explain why matrix cracking and interfacial debonding were significantly more pronounced in the single-fiber specimens.

In essence, single-fiber composite tests have offered robust methodologies for qualitative assessment of the fiber-matrix interface for years. They allow comparison between different material systems or material systems with the same constituents but, for instance, with distinct surface treatments. However, our findings suggest that single-fiber model specimens are not representative of multi-fiber composites. Hence, they should be used cautiously to characterize interfacial damage mechanisms for a specific material system or to provide interfacial properties for numerical models.

Further research needs to be conducted to elaborate on the primary reasons driving the differences between different specimen types and to allow the testing and development of current hypotheses. Future studies should be undertaken to measure the local strain in the matrix around fiber breaks in single-fiber and multi-fiber composites using digital volume correlation. The resulting 3D strain maps will also provide valuable insights into the strain recovery in broken fibers. Simultaneously, the 3D strain maps can act as the references for the output of numerical models that allow parametric exploration of the interface properties. This is the long-term objective of this study, which is critical considering the representativeness doubts surrounding single-fiber composite tests.

Experimental section

Materials

Two types of resins were used as matrix: (1) SR8500 – KTA313 two-component epoxy, produced by Sicomin Epoxy Systems, embedded with 1.5 vol.% barium titanate particles ($BaTiO_3$, 400 nm, near-spherical shape), produced by US Research Nanomaterials, Inc, (2) #350 series epoxy, embedded with silicon dioxide particles (SiO_2, 500 nm, near-spherical shape) produced by Mitsubishi Chemical Corporation. Three fiber types were used: (1) TORAYCA® T700SC-12000-50C carbon fiber from Toray Industries, Inc., (2) MRZ65-18000 carbon fiber from Mitsubishi Chemical Corporation, and (3) Advantex® R25HX14 glass fiber from 3B Fiberglass.

Particle-doped matrix preparation

The polymer matrix in all specimen types was doped with nanoparticles. The particles were embedded as a random speckle pattern required for digital volume correlation. Digital volume correlation is a full-field strain measurement technique often combined with computed tomography [32]. For composites, it has been used to provide local strain states linked with damage mechanisms in various loading conditions [33, 34]. DVC is not employed in this paper and, therefore, will not be discussed further.

The detailed matrix preparation procedure for producing the particle-doped matrix is described in [35]. For the carbon and glass single-fiber composites, as well as the glass multi-fiber composite, the matrix was doped with 1.5 vol.% $BaTiO_3$ [35]. For the carbon multi-fiber composite case, the matrix was doped with 10 wt.% SiO_2 [36]. Particle concentrations were selected to minimally impact the matrix system's mechanical and rheological behavior, as verified in [35, 36].

Carbon and glass single-fiber specimens design and manufacturing

A manual hot press was used to produce single-fiber specimens. Individual fibers were extracted from a fiber tow and attached to a copper spacer (a rectangular frame made of copper foil) using 30 μm thin Kapton tape. Grooves made by a scalpel guided the fiber placement on the spacer's surface. The copper spacer had a thickness of 150 μm. The groove spacing (and therefore fiber spacing) was 1 mm. The spacer's inner dimensions were 110 × 135 mm^2. A second identical spacer was deposited on top, thereby sandwiching the

fibers in the midplane. The configuration was then placed inside the press. 6 ml of prepared particle-doped epoxy resin was poured into the middle of the spacers using a syringe. The epoxy volume corresponded to the volume encapsulated by the two spacers (110 × 135 × 0.3 mm^3). The press was then closed using a manually driven spindle, compacting the spacers with the encapsulated epoxy via the top and bottom platens. The resin was cured for 4 hours and at a maximum temperature of 120 ℃. After curing, the thin resin film (thickness ~300 μm) was laser cut into a specimen with a notch on both sides, with the fiber located longitudinally in the middle of the notched region (Figure 1b).

Carbon and glass multi-fiber specimens design and manufacturing

Carbon: [90°/0°]s cross-ply laminates of carbon fiber prepreg were produced by Mitsubishi Chemical Corporation with a total thickness of ~0.5 mm. Curing followed the standard aerospace autoclave cycle to the manufacturer's specifications.

Glass: A prepreg drumwinder was used for glass fiber composite prepreg production. The system is based on a dual-axis winder where a drum rotates while translating in the transverse direction [35]. The detailed production process is given in [37]. With each drumwinding run, a unidirectional sheet of 210 × 30 cm^2 was produced. The sheets were then cut into 30 × 30 cm^2 unidirectional patches, which were stacked into a 90°/0°/90° layup. Curing proceeded in an autoclave for 280 minutes at an overpressure of 5 bar, a maximum temperature of 120 ℃, and an applied vacuum of -0.75 bar.

The produced glass and carbon laminates were machined via waterjet cut, following the specimen geometry outlined in Figure 1c. Both ends of the specimen were attached with 1.5 mm thick aluminium tabs to facilitate proper testing conditions.

Synchrotron beamline choice

The ID16B nano-analysis beamline [38] at the European Synchrotron Radiation Facility (ESRF) was chosen for the *in-situ* tests for four reasons. First, it offers *in-situ* loading capabilities, allowing 4D damage monitoring [39]. Second, ID16B provides an X-ray nano-tomography technique with a characteristic pixel size down to 25 nm. Additionally, the pixel size can be tuned by changing the position of the sample between the source and the detector. This ability relates to the conical nature of the ID16B beam created by Kirkpatrick–Baez (KB) mirrors. Third, the nano-tomography setup allows holo-tomography scans [40]. This 3D phase contrast imaging technique enhances phase boundaries by acquiring multiple tomograms at different propagation distances, enabling the algorithm to reconstruct the phase information with an enhanced signal-to-noise ratio. This feature is highly beneficial in this study due to the critical role of the phase boundary (= fiber-matrix interface). Furthermore, the holo-tomography technique is superior in spatial resolution among different X-ray phase contrast imaging techniques [41]. Fourth, the high brilliance and stability of the beam enable fast acquisition times (< 20 seconds). Slow acquisition is often associated with sample stress relaxation, which can directly influence image quality due to motion artifacts.

In-situ loading rig

To conduct the *in-situ* experiments at ID16B, a dedicated loading rig equipped with a 1 kN load cell was designed and manufactured in-house. The rig was designed following the restrictions of the beamline in terms of weight (< 500 g) and dimensions (i.e. the maximum distance from the bottom of the base plate to the centre of the region of interest ~ 50 mm). The rig's top part and base were made from aluminium to comply with the weight restriction. The support tube was made from polymethyl methacrylate (PMMA).

Strength characterization

Before conducting the experiments at ESRF, *n* number of specimens per configuration were tested in-house to obtain an indicative value for the UTS. The measured UTS corresponds to the geometry of the notch for the respective specimen type. The UTS was 70.3 ± 1.9 MPa (n = 15) for the single-fiber specimens, 270 ± 35 MPa (n = 4) for the glass multi-fiber composite specimens, and 1200 ± 80 MPa (n = 4) for the carbon multi-fiber composite specimens. At ID16B, scans were acquired at predetermined load levels corresponding to percentages of the estimated UTS based on each specimen's cross-section area. Once the specimen failed, the loading steps were recalculated based on the real UTS value. The scans were acquired at stress levels ranging from 5% to 99%UTS.

In-situ holo-tomography acquisition

For consistency, the scan acquisition parameters were constant across all specimen types and loading steps: beam = pink beam at 29.6 keV, detector: PCOedge 4.2 CLHS (2048 × 2048 px^2), beam flux = 2.1 × 10^{12} ph/s, exposure time = 10 ms, 2505 projections, and pixel size = 150 nm. Two scans were acquired sequentially for all multi-fiber composite and glass single-fiber specimens. The two scans correspond to two partially overlapping FOVs (overlapping length = 250 pixels), providing a larger FOV (3846 × 2048 px^2). This increase in FOV size helped to investigate the extent of specific failure characteristics, such as the damaged volume around fiber breaks. The same strategy was not chosen for the carbon single-fiber specimens since carbon fibers are known to exhibit much shorter critical lengths.

In-situ holo-tomography reconstruction

Scans were reconstructed via a multi-step procedure, which included (a) alignment, (b) phase retrieval, (c) tomographic reconstruction, and (d) ring artifact filtering [39]. The alignment step is applied to the acquired projections of the four distinct holograms captured at specific sample-to-detector distances. The alignment of each projection accounts for scaling due to magnification, horizontal and vertical displacement. After the projections were aligned, the phase retrieval step was conducted using an in-house developed octave script (GNU Octave programming language) [40]. A multi-distance Paganin approach was used to retrieve the phases using a δ/β ratio (real /imaginary part of the refraction index) equal to 425. Subsequently, the retrieved phase maps were used for tomographic reconstruction using the ESRF software PyHST2 [42]. Lastly, a ring filter artefact was applied to the reconstructed slices.

Tomogram image analysis

The obtained 16-bit 3D images were first converted to 8-bit in Fiji ImageJ software [43]. Using the same software, the volumes corresponding to single-fiber specimens were cropped to a smaller volume of interest for faster post-processing. The cropped volumes encapsulated only the single fiber and the associated damage phenomena around it, such as matrix cracks, if present. No cropping was executed for the multi-fiber composite cases since the entire volume was deemed useful for analysis. Subsequently, feature detection and quantification were performed using the commercial software Avizo v2023.2 (ThermoFisher Scientific).

For certain parameters, thresholding operations were performed. We note that segmentation is prone to reducing the fiber cross-sections and that fiber diameters measured with different techniques can show slightly higher values [44]. Furthermore, it is worth noting that thresholding operations are better suited for glass-fiber than carbon-fiber composites due to their relatively large greyscale contrast with the epoxy matrix as well as their larger diameters. However, considering the resolution of the scans and the technique via which they were acquired, we anticipate segmentation-related errors to be negligible.

The following parameters were extracted:

(a) *Fiber diameter* (d_f): For single-fiber composites, the fiber diameter was quantified using the first acquired tomogram. An average diameter was calculated using five equally spaced XY slices across the volume (= slices 0, 400, 800, 1200, and 1600). For multi-fiber composites, the maximum, minimum, average and standard deviation of the diameter were quantified as follows: First, using a random XY slice of the scan acquired at the lowest load level, the fibers are segmented using the *interactive thresholding* tool in the Avizo software. Subsequently, using the *label analysis* tool, a surface area is calculated for each fiber. Then, assuming the fibers are perfectly circular, the diameter values are being extracted.

(b) *Apparent critical length* (l_c): This parameter depicts the distance between the endpoints of two adjacent fiber breaks. The endpoints are detected by visualizing the XY slices, corresponding to orthogonal planes perpendicular to the fiber axis. The measurement relies on manually finding the first slice where the fiber appears intact. This consideration is more important for glass fibers, which often exhibit a conical or tapered fracture plane when they break.

(c) *Debond length* (l_d): Using the XZ slices, corresponding to planes parallel to the fiber axis, the debonded length is measured from the slice indicating the fiber break's endpoint to the last slice where the debond is visible along the fiber at any given circumferential position.

(d) *Interdebond length* (l_{id}): The parameter depicts the intact distance between the endpoints of two adjacent debonds. The distance is measured using the last XZ slices, in which the respective debond is visible around the fiber at any circumferential position.

(e) *Matrix crack volume* (V_{tmc}): This quantity is extracted by segmenting the entire matrix crack (via *interactive thresholding*) and calculating the volume (via *label analysis*) in Avizo. Only the volume present

beyond the fiber circumference is included in the calculation to avoid including the volume corresponding to the fiber break opening.

(f) *Maximum transverse propagation* (D_{tmc}): This quantity is a length that refers to the maximum radial propagation of the crack inside the matrix. It is measured by finding the XY slice where the crack has extended outwards the most. The measurement's starting point corresponds to the fiber's outer surface.

(g) *Number of and distance between fiber breaks*: For multi-fiber composites, fiber breaks are counted manually by visualizing the XY slices one by one (Fiji ImageJ software). We do not use segmentation to obtain this number to avoid instances where connecting (co-planar) fiber breaks are assumed to be one entity. As soon as a fiber break is detected, we record the XY slice (Z coordinate) corresponding to the center of the fiber break opening, as well as the X and Y coordinates corresponding to the center of the fiber axis. Based on these coordinates, we calculate the longitudinal distance (Z) and radial distances between fiber breaks (X, Y).

(h) *Fiber volume fraction*: For multi-fiber composites, the fiber volume fraction is estimated using the Avizo software as follows. Firstly, five XZ slices, spread across the entire volume, are randomly chosen. In each slice, a mask is created using the *interactive thresholding* tool in Avizo, where the whole volume is thresholded. In other words, all pixels now have a value of 1 in the binary scale. Next, a second mask is created on the same XY slice. This time, only the fibers are segmented. The pixel ratio between the two masks is then automatically calculated using the *volume fraction* tool in the Avizo software. The average value between the five slices is considered as the measured fiber volume fraction. All XY slices visualize nearly the same fiber arrangement. This is because the imaged FOV only includes the 0° ply, which consists of highly aligned unidirectional fibers. This consideration, along with the high spatial resolution of the scans, leads to a relatively precise fiber volume fraction estimate using the proposed strategy.

Acknowledgments

We would like to acknowledge the KU Leuven Research Council for project C14/21/076 and the Research Foundation Flanders for the postdoctoral fellowships ToughImage (126342IN), BIOPTOUGH (12B0624N), and COCOMI (1231322N). We acknowledge the European Synchrotron Radiation Facility (ESRF) for the provision of synchrotron radiation facilities at the ID16B beamline under proposal number MA5729. We would like to acknowledge the contributions from the Mitsubishi Chemical Corporation (Advanced Molding and Composites Laboratory, Aichi R&D centre, Japan) and the dedicated MCC scientists – Mr. Fukuhara Yasuhiro, Mr. Takano Tsuneo, Mr. Sugiura Naoki – for their sponsorship, material supplies, and technical support.

References

[1] AhmadvashAghbash S, Verpoest I, Swolfs Y, Mehdikhani M. Methods and models for fibre–matrix interface characterisation in fibre-reinforced polymers: a review. International Materials Reviews. 2023;68(8):1245-319.

[2] Tripathi D, Jones FR. Single fibre fragmentation test for assessing adhesion in fibre reinforced composites. Journal of Materials Science. 1998;33:1-16.

[3] Piggott MR. The single-fibre pull-out method: its advantages, interpretation and experimental realization. Composite Interfaces. 1993;1(3):211-23.

[4] Gaur U, Miller, B. Microbond Method for Determination of the Shear Strength of a Fiber/Resin Interface: Evaluation of Experimental Parameters Composites Science and Technology. 1989;34:35-51.

[5] Medina M C, Molina-Aldareguía JM, González C, Melendrez MF, Flores P, Llorca J. Comparison of push-in and push-out tests for measuring interfacial shear strength in nano-reinforced composite materials. Journal of Composite Materials. 2015;50(12):1651-9.

[6] Pitkethly MJ, Favre JP, Gaur G, Jakubowski J, Mudrich SF, Caldwell DL, et al. A round-robin programme on interfacial test methods. Composites Science and Technology. 1993;48:205-14.

[7] Klavzer N, Gayot SF, Coulombier M, Nysten B, Pardoen T. Nanoscale digital image correlation at elementary fibre/matrix level in polymer–based composites. Composites Part A: Applied Science and Manufacturing. 2023;168.

[8] AhmadvashAghbash S, Breite C, Mehdikhani M, Swolfs Y. Longitudinal debonding in unidirectional fibre-reinforced composites: Numerical analysis of the effect of interfacial properties. Composites Science and Technology. 2022;218.

[9] Swolfs Y, Gorbatikh L, Romanov V, Orlova S, Lomov SV, Verpoest I. Stress concentrations in an impregnated fibre bundle with random fibre packing. Composites Science and Technology. 2013;74:113-20.

[10] Johnson AC, Hayes SA, Jones FR. Data reduction methodologies for single fibre fragmentation test: Role of the interface and interphase. Composites Part A, Applied science and manufacturing. 2009;40(4):449-54.

[11] Wang C. Fracture mechanics of single-fibre pull-out test. Journal of Materials Science 1997;32:483-90.

[12] Schüller T, Bahr, U., Beckert, W., & Lauke, B. . Fracture mechanics analysis of the microbond test. Composites Part A: Applied Science and Manufacturing. 1997;29:1083-9.

[13] Feih S, Wonsyld K, Minzari D, Westermann P, Lilholt H. Testing procedure for the single fiber fragmentation test. Risø National Laboratory. 2004;Risø-R-1483(EN).

[14] Kim BW, Nairn JA. Observations of Fiber Fracture and Interfacial Debonding Phenomena Using the Fragmentation Test in Single Fiber Composites. Journal of composite materials. 2002;36(15):1825-58.

[15] Withers PJ, Bouman C, Carmignato S, Cnudde V, Grimaldi D, Hagen CK, et al. X-ray computed tomography. Nature Reviews Methods Primers. 2021;1(18):1-21.

[16] Swolfs Y, Morton H, Scott AE, Gorbatikh L, Reed PAS, Sinclair I, et al. Synchrotron radiation computed tomography for experimental validation of a tensile strength model for unidirectional fibre-reinforced composites. Composites Part A: Applied Science and Manufacturing. 2015;77:106-13.

[17] Schöberl E, Breite C, Melnikov A, Swolfs Y, Mavrogordato MN, Sinclair I, et al. Fibre-direction strain measurement in a composite ply under quasi-static tensile loading using Digital Volume Correlation and in situ Synchrotron Radiation Computed Tomography. Composites Part A: Applied Science and Manufacturing. 2020;137.

[18] Garcea SC, Mavrogordato MN, Scott AE, Sinclair I, Spearing SM. Fatigue micromechanism characterisation in carbon fibre reinforced polymers using synchrotron radiation computed tomography. Composites Science and Technology. 2014;99:23-30.

[19] Garcea SC, Sinclair I, Spearing SM. Fibre failure assessment in carbon fibre reinforced polymers under fatigue loading by synchrotron X-ray computed tomography. Composites Science and Technology. 2016;133:157-64.

[20] Bull DJ, Helfen L, Sinclair I, Spearing SM, Baumbach T. A comparison of multi-scale 3D X-ray tomographic inspection techniques for assessing carbon fibre composite impact damage. Composites Science and Technology. 2013;75:55-61.

[21] Maire E, Withers PJ. Quantitative X-ray tomography. International Materials Reviews. 2014;59(1):1-43.

[22] Johnson AC, Hayes SA, Jones FR. The role of matrix cracks and fibre/matrix debonding on the stress transfer between fibre and matrix in a single fibre fragmentation test. Composites Part A: Applied Science and Manufacturing. 2012;43(1):65-72.

[23] Pegoretti A, Accorsi M, Dibenedetto AT. Fracture toughness of the fibre-matrix interface in glass-epoxy composites. Journal of Materials Science. 1996;31:6145-53.

[24] A. Kelly WRT. Tensile properties of fibre-reinforced metals: copper/tungsten and copper/molybdenum. Journal of the Mechanics and Physics of Solids. 1965;13:329-50.

[25] Sørensen BF, Lilholt H. Fiber pull-out test and single fiber fragmentation test - analysis and modelling. IOP Conf Ser: Mater Sci Eng. 2016;139(1):12009.

[26] Li D, Lu C, Wu G, Yang Y, An F, Feng Z, et al. Structural heterogeneity and its influence on the tensile fracture of PAN-based carbon fibers. RSC Adv. 2014;4(105):60648-51.

[27] Dondeti S, Tippur HV. Cascading crack bifurcations in soda-lime glass: Quantification of fracture mechanics-based precursors using Digital Gradient Sensing. International Journal of Solids and Structures. 2022;234-235.

[28] Yang Y, Liu CT. Size effect on stability of shear-band propagation in bulk metallic glasses: an overview. Journal of Materials Science. 2012;47(1):55-67.

[29] Hobbiebrunken T, Fiedler B, Hojo M, Tanaka M. Experimental determination of the true epoxy resin strength using micro-scaled specimens. Composites Part A: Applied Science and Manufacturing. 2007;38(3):814-8.

[30] Sui XM, Tiwari M, Greenfeld I, Khalfin RL, Meeuw H, Fiedler B, et al. Extreme scale-dependent tensile properties of epoxy fibers. Express Polymer Letters. 2019;13(11):993-1003.

[31] Cech V, Palesch E, Lukes J. The glass fiber–polymer matrix interface/interphase characterized by nanoscale imaging techniques. Composites Science and Technology. 2013;83:22-6.

[32] Bay BK, Smith TS, Fyhrie DP, Saad M. Digital volume correlation: Three-dimensional strain mapping using X-ray tomography. Experimental Mechanics. 1999;39:217-26.

[33] Buljac A, Jailin C, Mendoza A, Neggers J, Tailandier-Thomas T, Bouterf A, et al. Digital Volume Correlation: Review of Progress and Challenges. Experimental Mechanics. 2018;58(5):661-708.

[34] Mehdikhani M, Breite C, Swolfs Y, Soete J, Wevers M, Lomov SV, et al. Digital volume correlation for meso/micro in-situ damage analysis in carbon fiber reinforced composites. Composites Science and Technology. 2021;213.

[35] Chatziathanasiou T, Demir O, Soete J, Breite C, Mehdikhani M, Diehl M, et al. Material representativeness of a polymer matrix doped with nanoparticles as the random speckle pattern for digital volume correlation of fibre-reinforced composites. Composites Part B: Engineering. 2024;276.

[36] Lee Y, Rankin, K., Patel, P., Basford, P., Furtado, C., Campos, P., Takeuchi, A., Uesugi, M., Wardle, B., Jalalvand, M., Mavrogordato, M.N., Spearing, S.M., Sinclair, I. . Internal Strain Sensing in carbon fibre composites via digital volume correlation and *in situ* synchrotron computed tomography. ICCM 23 International Conference on Composite Materials The ICC Belfast, Belfast, United Kingdom2023.

[37] Schöberl E, Breite C, Rosini S, Swolfs Y, Mavrogordato M, Sinclair I, et al. A novel particle-filled carbon-fibre reinforced polymer model composite tailored for the application of digital volume correlation and computed tomography. Journal of Composite Materials. 2021;55:1907-34.

[38] Martínez-Criado G, Villanova J, Tucoulou R, Salomon D, Suuronen J-P, Labouré S, et al. ID16B: a hard X-ray nanoprobe beamline at the ESRF for nano-analysis. Journal of Synchrotron Radiation. 2016;23(1):344-52.

[39] Villanova J, Daudin R, Lhuissier P, Jauffrès D, Lou S, Martin CL, et al. Fast in situ 3D nanoimaging: a new tool for dynamic characterization in materials science. Materials Today. 2017;20(7):354-9.

[40] Cloetens P, Ludwig W, Baruchel J, Van Dyck D, Van Landuyt J, Guigay JP, et al. Holotomography: Quantitative phase tomography with micrometer resolution using hard synchrotron radiation x rays. Applied Physics Letters. 1999;75(19):2912-4.

[41] Zanette I, Lang S, Rack A, Dominietto M, Langer M, Pfeiffer F, et al. Holotomography versus X-ray grating interferometry: A comparative study. Applied Physics Letters. 2013;103(24).

[42] Mirone A, Brun E, Gouillart E, Tafforeau P, Kieffer J. The PyHST2 hybrid distributed code for high speed tomographic reconstruction with iterative reconstruction and a priori knowledge capabilities. Nuclear Instruments and Methods in Physics Research Section B: Beam Interactions with Materials and Atoms. 2014;324:41-8.

[43] Schindelin J, Arganda-Carreras I, Frise E, Kaynig V, Longair M, Pietzsch T, et al. Fiji: an open-source platform for biological-image analysis. Nat Methods. 2012;9(7):676-82.

[44] Guo R, Alves M, Mehdikhani M, Breite C, Swolfs Y. Synthesising realistic 2D microstructures of unidirectional fibre-reinforced composites with a generative adversarial network. Composites Science and Technology. 2024;250.